Metrol. Meas. Syst., Vol. 27 (2020) No. 4, pp. 701–719
DOI: 10.24425/mms.2020.134848

METROLOGY AND MEASUREMENT SYSTEMS
Index 330930, ISSN 0860-8229
www.metrology.wat.edu.pl

WIDEBAND SPECTRAL EMISSION MEASUREMENTS FROM LASER-PRODUCED PLASMA EUV/SXR SOURCE BASED ON A DOUBLE GAS PUFF TARGET

Antony Jose Arikkatt, Przemysław Wachulak, Henryk Fiedorowicz, Andrzej Bartnik, Joanna Czwartos

Military University of Technology, Institute of Optoelectronics, ul. gen. Sylwestra Kaliskiego 2, 00-908 Warsaw, Poland
(✉ *antony.arikkatt@wat.edu.pl*, +48 729 623 734, *przemyslaw.wachulak@wat.edu.pl, henryk.fiedorowicz@wat.edu.pl, andrzej.bartnik@wat.edu.pl, joanna.czwartos@wat.edu.pl*)

Abstract

We present spectral emission characteristics from laser-plasma EUV/SXR sources produced by irradiation of < 1 J energy laser pulse on eleven different double stream gas puff targets, with most intense electronic transitions identified in the spectral range from 1 nm to 70 nm wavelength which corresponds to photon energy from 18 eV to 1240 eV. The spectra were obtained using grazing incidence and transmission spectrographs from laser-produced plasma emission, formed by the interaction of a laser beam with a double stream gas puff target. Laser pulses with a duration of 4 ns and energy of 650 mJ were used for the experiment. We present the results obtained from three different spectrometers in the wavelength ranges of SXR (1–5.5 nm), SXR/EUV (4–15.5 nm), and EUV (10–70 nm). In this paper, detailed information about the source, gas targets under investigation, the experimental setup, spectral measurements and the results are presented and discussed. Such data may be useful for the identification of adequate spectral emissions from gasses in the EUV and SXR wavelength ranges dedicated to various experiments (*i.e.* broadband emission for the X-ray coherence tomography XCT) or may be used for verification of magnetohydrodynamic plasma codes.

Keywords: Plasma Spectroscopy, X-ray coherence tomography, soft X-ray.

1. Introduction

The wavelengths in the range from ~0.1 nm to 10 nm of the electromagnetic spectrum, which corresponds to the energy range from ~120 eV to 12 keV, are defined as *soft X-rays* (SXR). Electromagnetic radiation with a wavelength from 10 nm to ~120 nm (photon energy ranges from 10–120 eV) is termed *Extreme Ultra-Violet* (EUV) [1]. Such radiations used in various applications are mainly produced using electric discharge tubes [2], capillary discharge lasers [3, 4] synchrotrons [5, 6], and *laser-produced plasma* (LPP) sources [7] including photoionization UV and EUV sources [8]. The LPP sources are based on creating plasma on a target by irradiating it with high energy laser pulses. Typically, solid [9, 10], liquid [11, 12], or gas puff [13, 14] are

used as targets for LPP sources. LPP sources are especially used in the development of EUV lithographic applications in high volume semiconductor manufacturing [15, 16].

One of recent developments in tabletop laser-plasma X-ray sources is based on double stream gas puff targets. A significant increase in EUV emission from double gas puff targets compared to that from single gas puff targets in similar laser and backing gas pressure conditions were successfully demonstrated [17]. While gas puff targets pose no problem with fragmented target debris which can damage or contaminate optics, as in the case of solid targets, their intensity of emissions is typically lower than that of solid or liquid targets. They have a significant advantage in terms of high repetition rates which can compensate for the lower emission in many applications. Numerous applications have been developed using this setup of double stream gas puff targets, including microscopy [18, 19], *near-edge X-ray absorption fine structure* (NEXAFS) spectroscopy [20], radiography [21] and surface processing of polymers [22]. Recently, a nanometre axial resolution *X-ray coherence tomography* (XCT) has been demonstrated using a *double gas puff target* (DGPT)-based laser-plasma X-ray source [23]. In a DGPT arrangement, an inner gas stream is surrounded by an outer gas stream with a very low atomic number element at a high pressure, which confines the flow of the inner gas and decreases its density gradient in the direction of the nozzle axis, Fig. 1a. This increases the target density in the laser-gas interaction region. There is a significant interest in maximizing output from laser-produced plasmas in different wavelength ranges meant for specific applications [24–26].

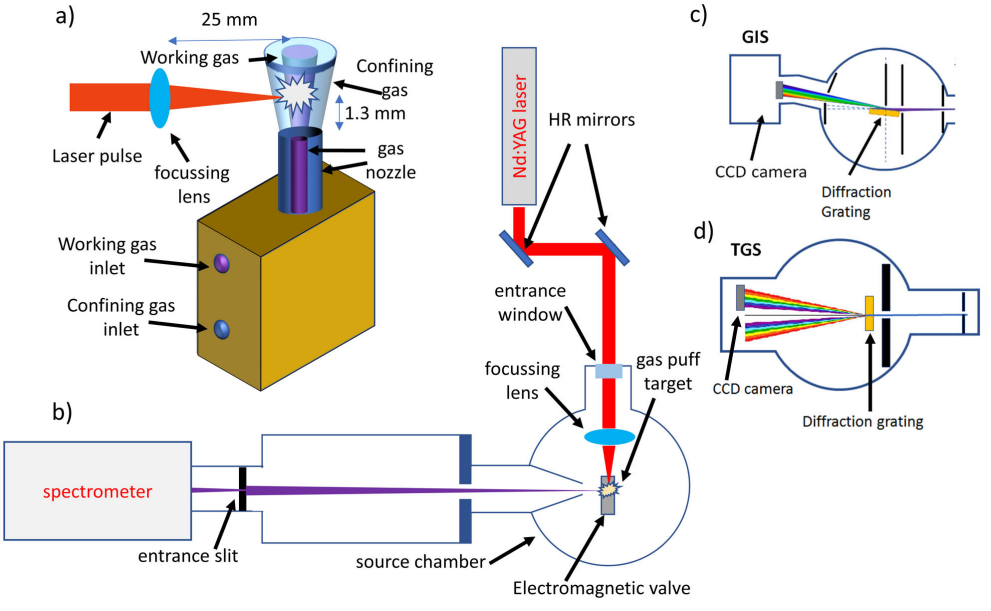

Fig. 1. Scheme of the double stream gas puff target (a), the experimental setup for EUV/SXR spectroscopic measurements (b), the scheme of grazing incidence spectrometer (c), and transmission grating spectrometer (d).

In the present work, wideband spectral emission measurements from such a laser-produced plasma source based on double stream gas puff target are reported. We examine the EUV/SXR radiation from eleven gases including gas mixtures in the wavelength range from 1 to 70 nm. We investigate spectral signatures of six elemental gases which are Ar, Ne, Kr, Xe, O_2, and N_2, compound gases namely SF_6, CO_2, and mixtures of gases which are Ar:N_2:O_2, CH_4:CO_2:N_2, and

Metrol. Meas. Syst., Vol. 27 (2020), No. 4, pp. 701–719
DOI: 10.24425/mms.2020.134848

Kr:Xe. Emissions from compound gases originate from the electronic transitions of constituent elements. This is advantageous in terms of investigating elements that are solids in their elemental form. Three different spectrometers with three different wavelength ranges were employed in the experiments. Spectra for each gas target are presented.

The presented work provides an initial qualitative description of spectral emission observed in double gas puff targets from eleven different gases. It provides a description of maximum ionization levels possible using double gas puff targets at the specific laser intensity and gas target conditions. The spectral emission reported in the work is not optimized for each wavelength range and application. Instead, it is a qualitative study that can provide insight into the emission properties of the double gas puff target in the spectral region mentioned.

The EUV/SXR range of the electromagnetic spectrum is an increasingly important research area and is more accessible due to advancements in compact sources and more efficient X-ray optics. Soft X-rays also include the "water-window" region ($\lambda = 2.3\ \text{nm} - 4.4\ \text{nm}$) in which water has a relatively low absorption coefficient, comparing to carbon. This property makes this wavelength range applicable to high-resolution imaging of biological samples [27]. Additionally, broadband sources are useful due to higher photon yield for *i.e.* contact microscopy [28, 29], or for the capability of adjusting the coherence length for *X-ray coherence tomography* (XCT) [30]. Moreover, spectroscopic studies in the EUV and SXR regions have attracted significant attention due to the wider scope they provide in understanding the electronic transitions and inner atomic structure of elements especially with higher atomic numbers through, *i.e.* the photoionization processes [31]. Characterization of plasma emissions in the EUV and SXR regions is extremely important in terms of development of applications based on these radiations. Additionally, another potential application of this work is modelling the LPP sources using magnetohydrodynamic codes.

2. Experimental data

2.1. Experimental setup

The experimental setup for the investigation of spectral emissions from an LPP source, with various gasses as targets, is depicted in Fig. 1b. The main components of the system are a pumping laser, a double stream gas puff target produced by an electromagnetic valve system positioned inside a vacuum chamber maintained at 10^{-3} mbar and three spectrometers for different EUV/SXR wavelength regions.

The pumping laser used in the experiment is an Nd:YAG laser (EKSPLA, NL303HT, Lithuania) which operates at 1064 nm wavelength. The generated laser pulse has a duration of 4 ns and an energy of 650 mJ with a repetition rate of 10 Hz. The laser is focused on the gas puff target using a lens of 25 mm focal distance. The position of the focusing lens was adjusted in such a way so as to focus the laser pulses on the axis of the nozzle producing the target and ~1.3 mm away from the nozzle itself, as shown in Fig. 1a. The interaction of the laser pulses with a double stream gas puff target transfers the pulse energy to the gas puff target to create laser plasma. The degree of ionization of investigated gases is proportional to the power density of the pumping, which for a 10 mm diameter laser beam, illuminating a 1/2 inch diameter lens that produces a focal spot of ~0.1 mm in diameter, is equal to 2.1×10^{12} W/cm^2.

A specially designed double nozzle provides the concentric double gas stream. The round inner nozzle has a diameter of 0.4 mm and the surrounding ring-shaped nozzle has an inner diameter of 0.7 mm and an outer diameter of 1.5 mm. The whole chamber is maintained at a high

vacuum to eliminate other atmospheric gases and to reduce the absorption of generated EUV and SXR radiation by residual gases which could affect the results. Various gasses were injected through the inner nozzle as working gas targets, while a confining gas was pulsed through the outer nozzle. Helium was used as the confining gas in the experiment as it does not have significant absorption in the EUV/SXR range. It is supplied at 6 bar pressure which confines the investigated gas supplied at 5 bar pressure.

The laser plasma source optimization procedures were done at various levels. Laser beam focusing was located on the axis of the nozzle, ~1.3 mm above it, to prevent damage from high-temperature plasma. The position of the nozzle in the horizontal plane was also adjusted to obtain maximum fluence on the spectrometer's entrance slit. Optimal supply pressures for both gases were also found out to produce a maximum density of working gas in the interaction region which, in turn, produces high fluence. The optimization of synchronization of valve control with respect to the arrival of the laser pulse is necessary to introduce maximum (optimal) emission from plasma in each wavelength range. More details about the EUV/SXR LPP source and its optimization can be found in [32].

In this experiment, three different spectrometers were used for measuring the EUV and SXR output emitted from plasma in the direction perpendicular to the nozzle axis and the direction of the pumping laser beam. A *grazing incidence spectrometer* (GIS) with an entrance slit width of 12 μm and a diffraction grating with 2400 l/mm line density is used to measure the SXR radiation in the wavelength range from 1 to 5.5 nm. The diagram of the spectrometer was shown in Fig. 1c. For spectral recording, a back-illuminated CCD camera was used (GE 2048 2048BI, greateyes GmbH, Germany), with 13×13 μm^2 pixel size and a 2 k×2 k chip and was cooled down to −20 °C during acquisition.

In the wavelength range from 4 to 15.5 nm (called EUV I), a *transmission grating spectrometer* (TGS), with its diagram shown in Fig. 1d, was employed, with an entrance slit of 30 μm and 5000 l/mm diffraction grating. For data recording, a back-illuminated CCD camera was used (DO934N BN, Andor, UK), with 13×13 μm^2 pixel size and a 1 k×1 k chip and was cooled down to 0 °C during acquisition.

Finally, to measure the spectra in the wavelength range from 10 to 70 nm (called EUV II), a GIS was used, with an entrance slit of 25 μm and diffraction grating with a density of 450 l/mm. In this case, for data recording a back-illuminated CCD camera was used (PIXIS:400, Princeton Instruments, USA), with 20×20 μm^2 pixel size and 1340×400 chip, and was cooled down to −20 °C during acquisition.

To measure the intensity of spectral lines the selected region along the dispersion direction is integrated over many CCD lines to get a clear spectral line plot with a higher signal to noise ratio. For the SXR spectrometer, 250 CCD lines are averaged to get spectral line intensity. For EUV I and EUV II spectrometers 90 and 20 CCD lines, respectively, are averaged to obtain spectral line plot.

2.2. Spectrometer calibration

The calibration of spectrometers is one of the major steps in the experiment. Since three different spectrometers were used, each one of them was calibrated individually, according to its characteristics. Isolated characteristic emission lines from different elements were used for the calibration of the spectrometers. The details of such characteristic emission lines were found using various databases [33, 34]. The mapping of the pixel number of the camera to the wavelength was done by fitting a second-degree polynomial function to minimize the R-square factor. Using the calibration lines identified in the spectral data, a polynomial fit that maps every pixel

Metrol. Meas. Syst., Vol. 27 (2020), No. 4, pp. 701–719
DOI: 10.24425/mms.2020.134848

in the dispersion direction to the corresponding wavelength was performed. The spectrometer calibration data is indicated in Table 1. All the fits were found to have fit values with the R^2 factor approaching 1.

Table 1. Calibration data of the spectrometers *

SXR spectrometer, λ = 1–5 nm, GIS, resolving power E/ΔE = 855							
Pixel Position	740	948	1034	1078	1221	1846	1858
Wavelength (nm)	1.680	2.160	2.377	2.489	2.879	4.873	4.918
Spectral line	F-VIII	O-VII	N-VI	N-VI	N-VI	Ar-IX	Ar-IX
Fitting	$\lambda = 0.4145 + 0.0012x + 6.3805E - 7x^2$, $1 - R^2 = 1.7 \cdot 10^{-6}$						

EUV I spectrometer, λ = 4–15.5 nm, TGS, resolving power E/ΔE = 491									
Pixel Position	33	81	256	373	460	576	613	743	940
Wavelength(nm)	4.743	5.295	7.266	8.582	9.578	10.905	11.294	12.78	15.00
Spectral line	S-IX	S-VIII	S-VII	F-VII	F-VII	F-VI	F-VII	F-VII	O-VI
Fitting	$\lambda = 4.3611 + 0.0113x - 9.12E - 8x^2$, $1 - R^2 = 2.9 \cdot 10^{-5}$								

EUV II spectrometer, λ = 10–70 nm, GIS, resolving power E/ΔE = 772									
Pixel Position	164	203	223	315	398	438	902	1046	1187
Wavelength(nm)	14.03	15.80	16.69	20.93	24.77	26.63	48.75	55.83	62.79
Spectral line	N-V	N-V	N-V	N-V	N-V	N-V	N-V [III]	N-V [III]	N-V [III]
Fitting	$\lambda = 6.6176 + 0.0447x + 2.18E - 6x^2$, $1 - R^2 = 8.3 \cdot 10^{-7}$								

*wavelengths and spectral lines are from the NIST database [33].

Considering the isolated lines and measuring their FWHM, the maximum resolving powers of the spectrometers were estimated. The maximum resolution for the SXR (GIS) spectrometer was E/ΔE = 855, taking into account a line at λ = 4.874 nm of Ar ions, with an FWHM of 0.0057 nm, for the EUV I spectrometer (TGS) as E/ΔE = 491, taking into account a Ne line at λ = 7.865 nm, with an FWHM of 0.0160 nm, and for EUV II spectrometer (GIS) E/ΔE = 772, taking into account another Ar line at λ = 56.6 nm, with an FWHM of 0.0733 nm. The calibration data for all the spectrometers and lines used for the calibration are listed in Table 1.

3. Spectroscopic measurements

The spectral results in the range of wavelengths from 1 to 70 nm, obtained using three spectrometers for eleven gases are presented herein. Transition wavelengths were identified using the *National Institute of Standards and Technology* (NIST) database [33]. The most intense lines and bands (transition arrays) are identified in every spectrum. In Figs. 2–12, we labelled the most intense lines by their reference wavelength obtained from the NIST spectral database with corresponding observed (calibrated) wavelengths in the parenthesis. The diffraction order other than the first one is indicated in the square brackets. In all the results shown below, emissions from the SXR and EUV I spectral ranges are depicted in Fig. a, b respectively. The emission data from the EUV II range (10–70 nm) is divided into two separate plots in the range of 10–32 nm and 30–70 nm and shown in Fig. c, d, respectively, for better identification and visibility of lines in the wider spectral range. The range of the spectrometers was chosen to have an

overlapped spectral region. This is done intentionally for better calibration of spectrometers. In the three spectrometers, the overlapping wavelength ranges are from 4 nm to 5.5 nm and from 10 nm to 15.5 nm. Two sets of data, from different spectrometers, are available in this range for spectral alignment and possible spectral stitching. Due to previously measured $\Delta\lambda$ values for each spectrometer, the spectral measurements in Figs. 2–12 were provided with 0.01 nm accuracy for the SXR spectrometer and 0.1 nm for both EUV spectrometers.

3.1. Atomic and molecular gases

Spectral emissions from the nitrogen gas puff target in the EUV/SXR range are shown in Fig. 2a–d. Nitrogen (Z = 7) has a few narrow spectral lines corresponding to N-VI ionization in the SXR range, as seen in Fig. 2a, which can be typically used for high-resolution X-ray microscopy in the "water-window" [19]. The lines identified are transitions between $1s^2$ and 1s (2 to 5)p energy levels and the prominent line in the group is at 2.88 nm related to $1s^2 - 1s\,2p$ transition. In the EUV I range as shown in Fig. 2b we did not detect any lines except second-order diffraction corresponding to N-VI ionization (λ = 2.8787 nm) line at λ = 5.7 nm. In the EUV II range, we identified several spectral lines corresponding to N-III to N-V ionization levels with their third diffraction orders which are depicted in Fig. 2c, d. In the N-V (Li Like) ionization stage, we identified nine prominent lines which are the transitions between energy levels of configurations $1s^2\ 2s - 1s^2$ (3 to 6)p, $1s^2\ 2p - 1s^2\ 3s$ and $1s^2\ 2p - 1s^2$ (3 to 6)d.

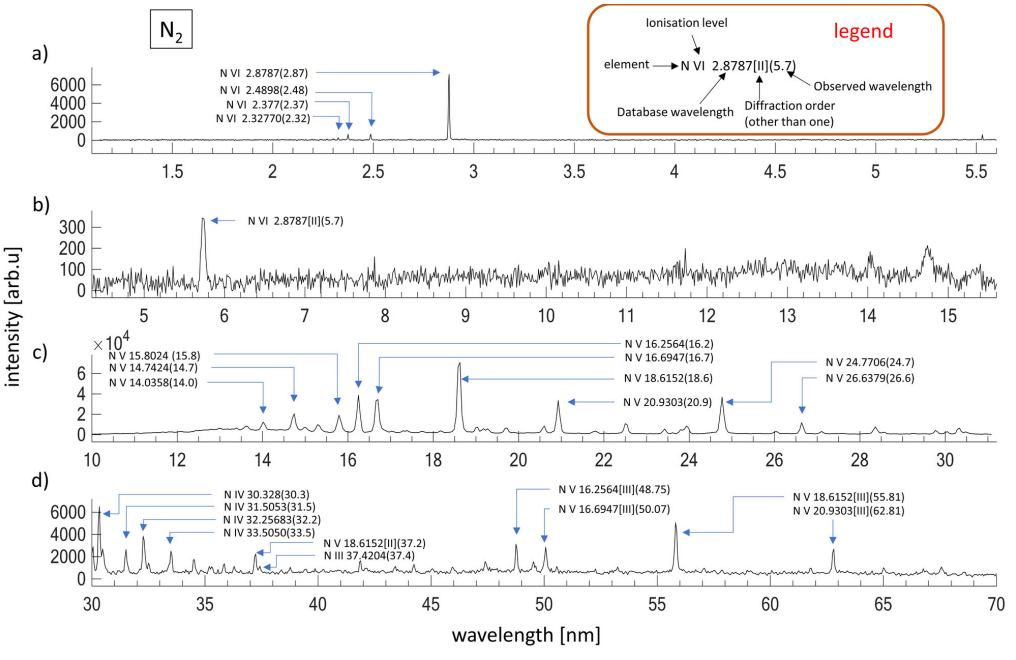

Fig. 2. Nitrogen spectra in the wavelength range of: a) 1–5 nm, b) 4–15 nm, c) 10–32 nm, and d) 30–70 nm.

The spectral emissions from oxygen (Z = 8) gas puff target are depicted in Fig. 3a–d. As oxygen is a low atomic number element, we identified only one significant emission line in the SXR range at 2.16 nm corresponding to O-VII ion transition between $1s^2 - 1s\,2p$ configurations.

Metrol. Meas. Syst., Vol. 27 (2020), No. 4, pp. 701–719
DOI: 10.24425/mms.2020.134848

In the EUV I range, the detected emission lines are from O-VI ionization level, and in the EUV II range, several emission lines corresponding to O-V and O-VI ionization levels and their third diffraction orders were detected. Significant lines detected in the EUV II range are $1s^2\,2s - 1s^2\,3p$, $1s^2\,2p - 1s^2\,3s$ and $1s^2\,2p - 1s^2$ (3 to 5)d corresponding to O-VI ionisations stages and two transitions between $1s^2\,2s\,2p - 1s^2\,2s$ (3,4)d configuration levels corresponding to O-V ionization stage. Since the oxygen has a low atomic number, we could see that the emissions occurred mostly in single and isolated lines.

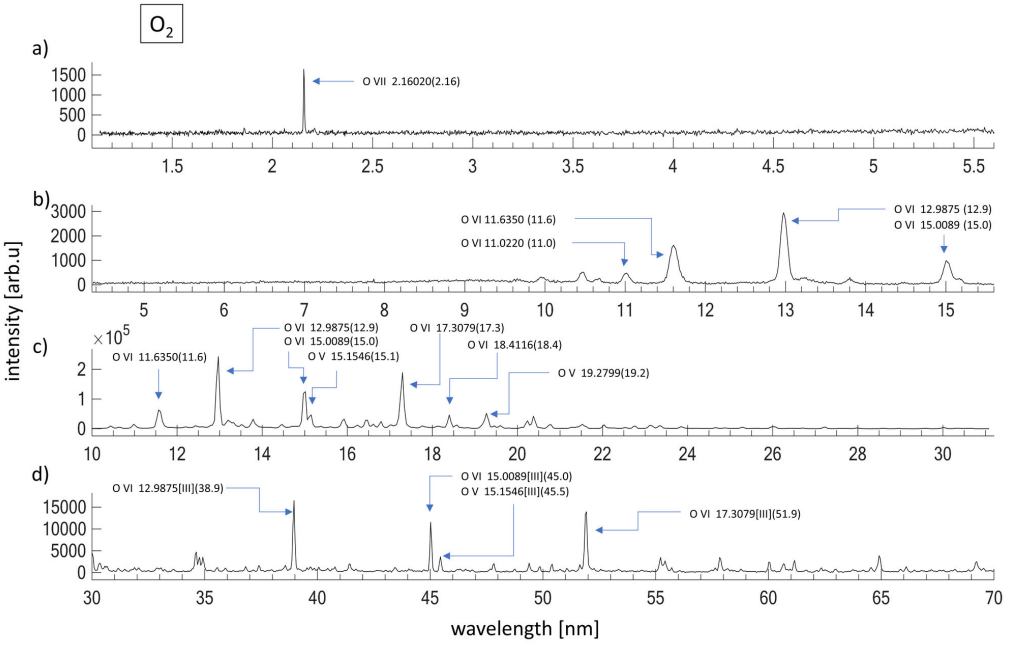

Fig. 3. Oxygen spectra in the wavelength range of: a) 1–5 nm, b) 4–15 nm, c) 10–32 nm, and d) 30–70 nm.

The spectral emission from the neon (Z = 10) gas puff target is depicted in Fig. 4a–d. According to the NIST database, the emission in the 1–5 nm spectral range can originate from Ne-VIII (λ = 1.16 nm to 1.38 nm and 1.42 nm) and from Ne-VII (λ = 1.38 nm to 1.39 nm) ions, however, at the achievable power density, these transitions could not be excited. We did not detect any significant emission lines for neon plasma in the SXR region, as Fig. 4a shows instrumental noise only. In the EUV I range we identified several lines related to Ne-VII and Ne-VIII ionization levels though the intensities were much lower. The identified prominent lines related to the Ne-VIII ionization stage transitions are between the levels $1s^2\,2p - 1s^2\,4s$, $1s^2\,2p - 1s^2$ (3 to 6)d, $1s^2\,2s - 1s^2$ (3 to 5)p and $1s\,2s\,2p - 1s\,2p\,3d$. With Ne-VII ionization stage in the EUV I range we identified two prominent lines related to the electron configuration levels $1s^2\,2s\,2p - 1s^2\,2s\,3d$ and $1s^2\,2p^2 - 1s^2\,2p\,3d$. In the EUV II spectral range, we identified several emission lines related to Ne-V to Ne-VIII ionization levels especially in the range of 10 – 20 nm. The emission lines depicted in Fig. 4d are just higher diffraction orders of the lines found in Fig. 4c.

The spectra obtained from the argon (Z = 18) are depicted in Fig. 5a–d. We can see the characteristic high-intensity lines of Ar-IX (database wavelengths: 4.87381 nm and 4.91848 nm) which are also used for the calibration of the spectrometer in the SXR range. We could detect

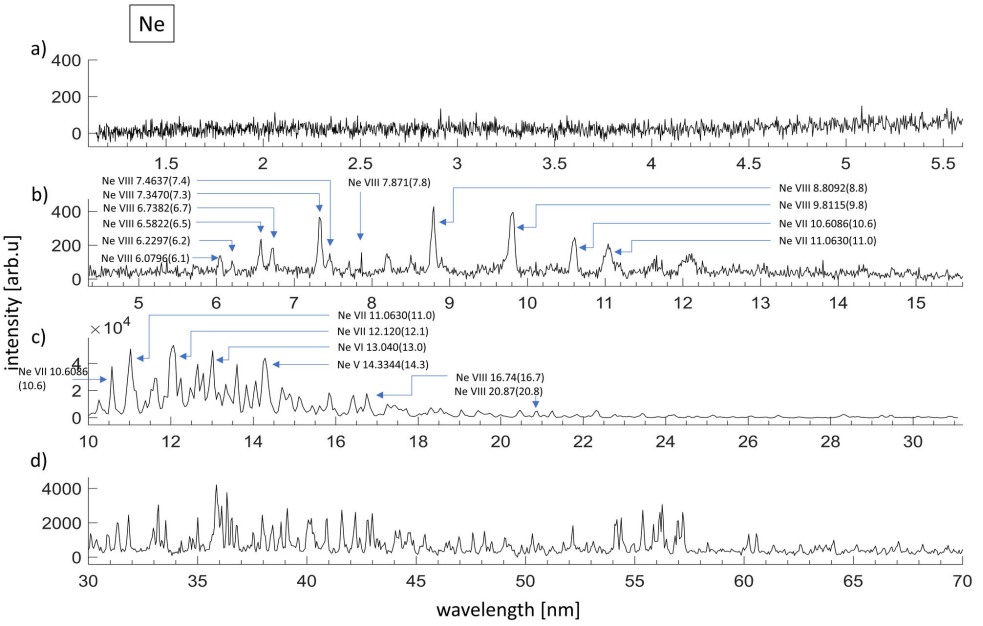

Fig. 4. Neon spectra in the wavelength range of: a) 1–5 nm, b) 4–15 nm, c) 10–32 nm, and d) 30–70 nm.

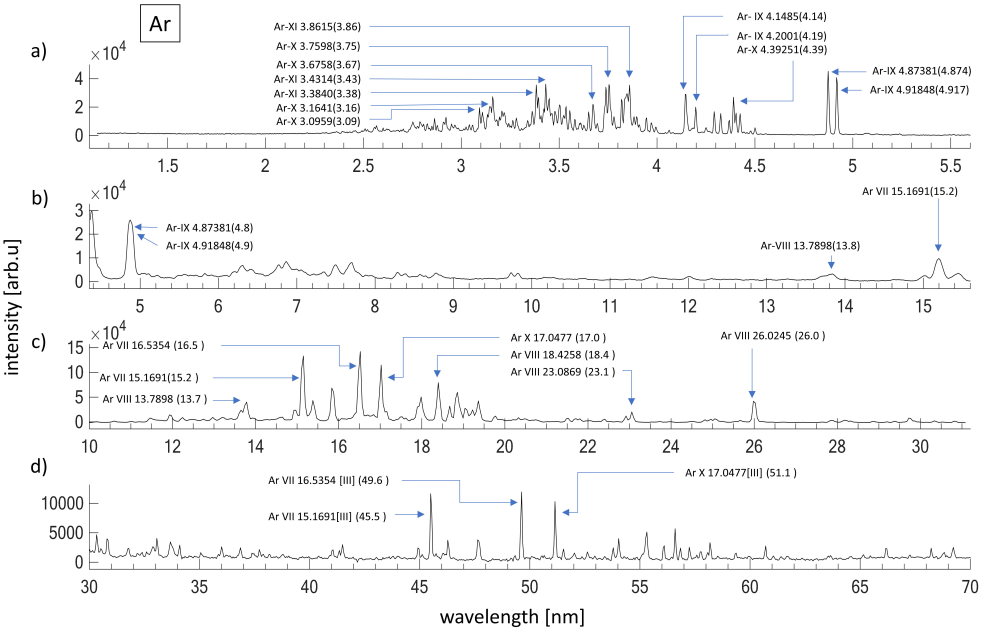

Fig. 5. Argon spectra in the wavelength range of: a) 1–5 nm, b) 4–15 nm, c) 10–32 nm, and d) 30–70 nm.

significant emission in the "water window" region between 2.33 and 4.40 nm which can be used in the imaging of organic materials using contact microscopy approach. We were able to identify emissions from Ar-IX to Ar-XI ionization levels in this range. The main lines identified corre-

Metrol. Meas. Syst., Vol. 27 (2020), No. 4, pp. 701–719
DOI: 10.24425/mms.2020.134848

sponding to Ar-IX ionization stages are transitions between energy levels $2s^2\ 2p^6 - 2s^2\ 2p^5\ 3s$ and $2s^2\ 2p^6 - 2s^2\ 2p^5\ 3d$, and from Ar-X ionization stages are transition between $2s^2\ 2p^5 - 2s^2\ 2p^4\ 4s$ and $2s^2\ 2p^5 - 2s^2\ 2p^4$ (3d to 5d). Related to Ar-XI ionization stage, the prominent lines identified are electron transitions between levels $2s^2\ 2p^4 - 2s^2\ 2p^3$ (3s,3d). In the EUV I range, due to lower resolution, we identified the above mentioned two characteristic lines merged as one peak at λ = 4.887 nm. In that range, we identified emissions from Ar-VII, Ar-VIII and Ar-IX ionization levels. In the EUV II range, we were able to detect emissions from Ar-VII to Ar-X ionization levels mostly in the range 12–20 nm. Furthermore, we detected only the third diffraction order of the mentioned lines which are labelled in Fig. 5d.

The spectra obtained from the krypton (Z = 36) gas target are provided in Fig. 6a–d. From the spectra, we found out that krypton produces a very broad emission band in the range of 3 to 20 nm. It is attributed to its higher atomic number and a larger number of possible transitions. With higher atomic numbers, the complexity of electronic sublevels increases and electronic levels are more a band-like structure, so-called transition arrays. In our experiment, we were able to identify several transition arrays, though beyond 20 nm some isolated spectral lines are also visible.

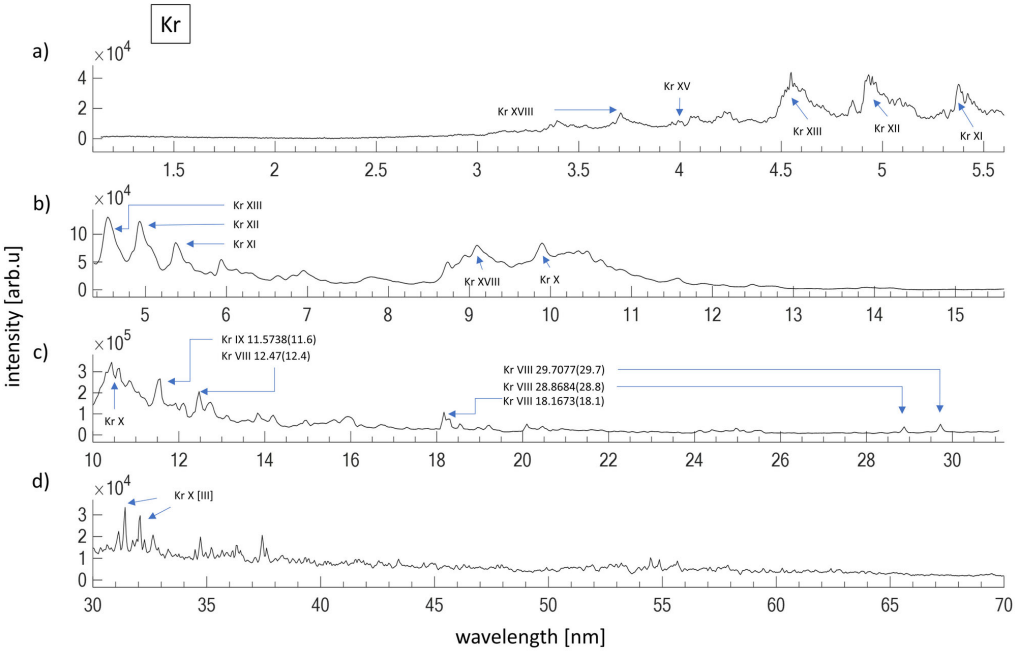

Fig. 6. Krypton spectra in the wavelength range of: a) 1–5 nm, b) 4–15 nm, c) 10–32 nm, and d) 30–70 nm.

In the SXR range, we identified bands corresponding to Kr-XI to Kr-XVIII ionization levels. In the EUV I range we identified spectral bands related to Kr-X to Kr-XIII ionization levels and in the EUV II range, we identified spectral lines on the top of a spectral band related to Kr-VIII and Kr-IX. The spectral characteristics around 12–15 nm are not clearly visible using the EUV I spectrometer but are more visible in the EUV II spectrometer results. The reason for this is due to the high difference in intensities. By analyzing the data from the mentioned region and plotting it separately, we were able to identify and match the data from both spectrometers.

Such broadband emission from Kr plasma in the SXR range was already employed in NEXAFS [20] and XCT [23] experiments. The results of a spectral investigation of the xenon gas (Z = 54) target are depicted in Fig. 7a–d. As expected from the previous investigations, xenon gas, due to a much higher atomic number, has the widest broadband emission compared to all other gases investigated in the experiment. Using the NIST database, we identified the spectral emission bands which are corresponding to the Xe ionization levels from Xe-XXVI and Xe-XXIX in the SXR range. In the EUV I range, we could identify a spectral band from 8 to 11 nm with high intensity which corresponds to Xe-VIII to Xe-X ionization levels. In the EUV II range, we could identify another broadband emission with high intensity from 14 to 20 nm. Due to the significant presence of third diffraction order and since Xe has a broader emission band we were able to detect significant signal in the region 30–70 nm which is depicted in Fig. 7d. The broadband emission from xenon makes it feasible for applications like the XCT in the EUV range. Since the spectrum is quasi-continuous, the identification of individual transition levels is extremely difficult.

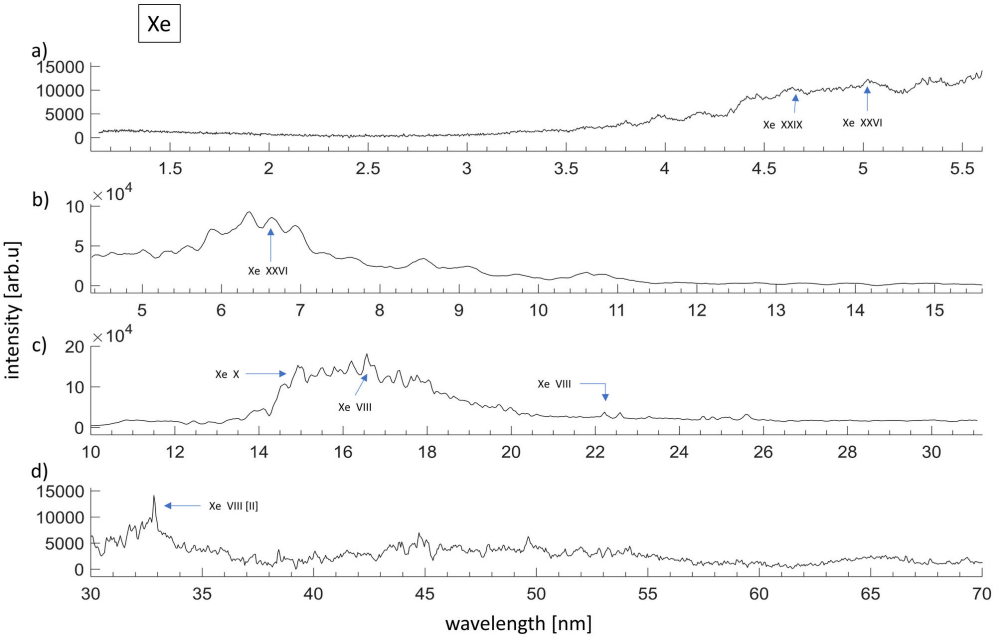

Fig. 7. Xenon spectra in the wavelength range of: a) 1–5 nm, b) 4–15 nm, c) 10–32 nm, and d) 30–70 nm.

3.2. Compound gases

Experimental results for carbon dioxide gas (C–Z = 6, O–Z = 8) as gas puff target are presented in Fig. 8a–d. In the SXR range, several bright carbon lines are detected. We identified emission lines related to C-V ($1s^2 - 1s$ (2–4)p) and C-VI (1s – 2,3p) ionization levels. It can be noticed that the C-V lines are significantly stronger than the C-VI lines. Also, the characteristic O-VII line at 2.16 nm can be noticed in the SXR range. In the EUV I range, we identified emissions related to C-V, C-VI, and O-VI ionization levels. In the EUV II range, we identified the emission from O-V and O-VI ionization levels and their third diffraction orders but could not detect significant emission from carbon.

Metrol. Meas. Syst., Vol. 27 (2020), No. 4, pp. 701–719
DOI: 10.24425/mms.2020.134848

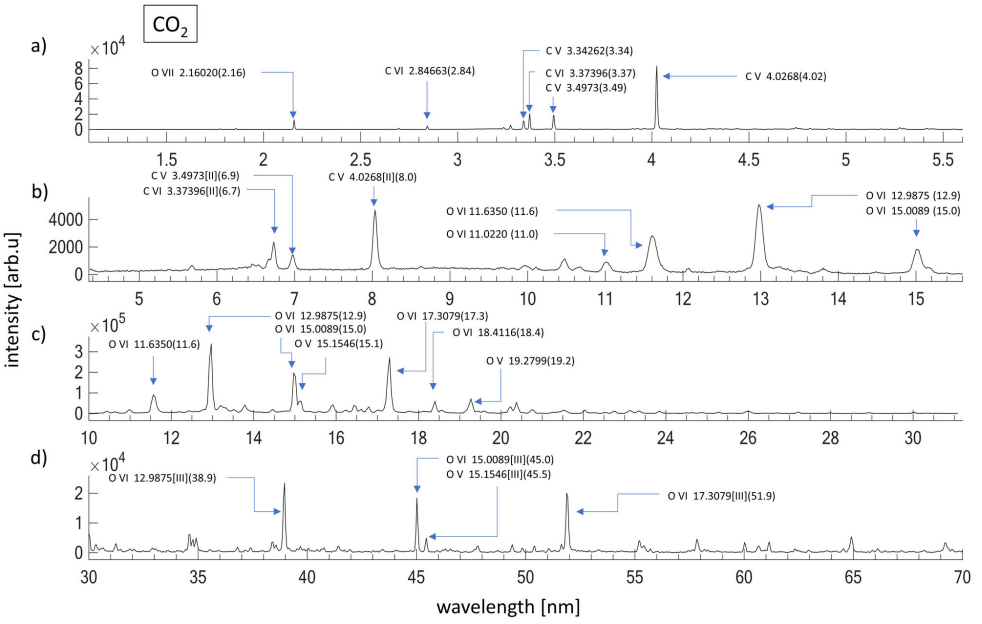

Fig. 8. CO_2 spectra in the wavelength range of: a) 1–5 nm, b) 4–15 nm, c) 10–32 nm, and d) 30–70 nm.

Emission from a compound gas SF_6 (S–Z = 16 and F–Z = 9) was analyzed using our LPP source and is depicted in Fig. 9a-d. In the SXR range, we identified the characteristic fluorine line at $\lambda = 1.6807$ nm corresponding to F-VIII ionization level which is the transition

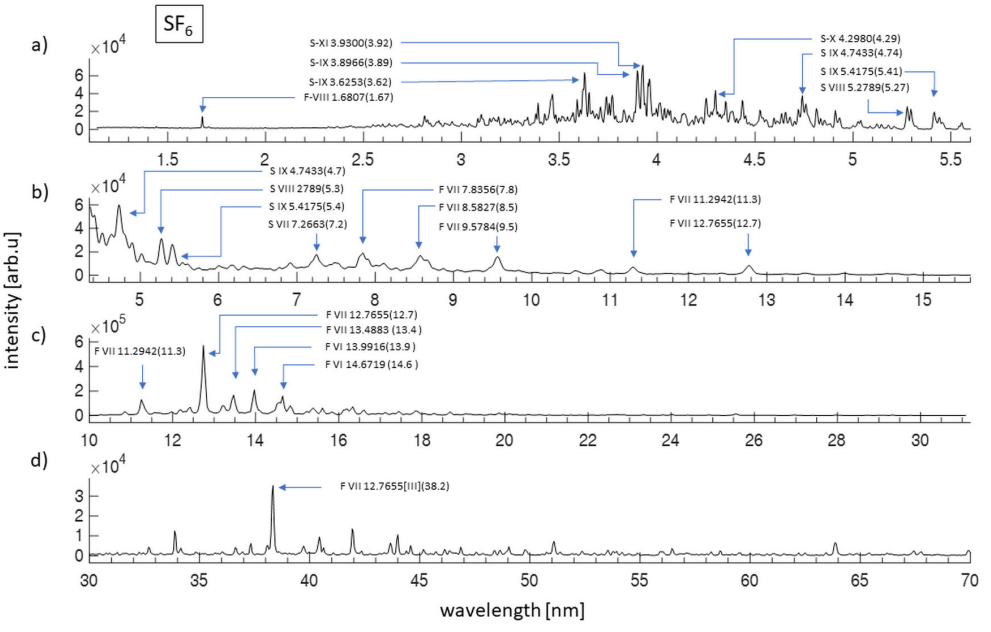

Fig. 9. SF_6 spectra in the wavelength range of: a) 1–5 nm, b) 4–15 nm, c) 10–32 nm, and d) 30–70 nm.

between configuration level $1s^2 - 1s\,2p$, used by us in the spectrometer calibration for this range as well as several lines related to the S-VIII to S-XI ionization levels. Prominent lines identified in this region include transitions between $2s^2\,2p^4 - 2s^2\,2p^3$ (3,4)d in S-IX ionization stage, $2s^2\,2p^3 - 2s^2\,2p^2\,3d$ configurations in S-X ionization stage and $2s^2\,2p^2 - 2s^2\,2p\,3d$ configurations in S-XI ionization stage.

We identified more sulfur lines than fluorine lines in the investigation of this compound since lower atomic number atoms have fewer lines towards the SXR region. In the EUV I spectral range emissions from F-VII and S-IX ionization levels were detected. Many fluorine transitions between configurations $1s^2\,2p - 1s^2$ (3–5)d and $1s\,^2 2s - 1s^2$ (3,5)p are identified related to F-VII ionization stage. In the EUV II range, we identified several spectral lines from F-VI and F-VII ionization levels and these are labelled in Fig. 9c.

3.3. Gas mixtures

Spectral emissions from a mixture of gases Kr:Xe (Kr–Z = 36 and Xe–Z = 54), in a volumetric ratio of 9:1, in comparison with contribution from individual constituent gasses are depicted in Fig. 10a–d. The main advantage of such a mixture is that it provides the spectral emissions of Kr and Xe, both having broadband emissions in the investigated SXR and EUV spectral ranges. In the SXR region, Kr emission dominates over the Xe emission, while in the EUV I range more broadband emission in the wavelength range from 4 to 11 nm is observed which is the results of complementary contributions of component gases. For comparison between the spectral emission from individual gases and mixtures, the spectra from individual gases are also shown in Fig. 10. A very intense peak related to Xe-XI ionization, at ~11 nm wavelength, is identified in the mixture which is absent in the emission from individual Xe. The absence of a peak in an individual Xe

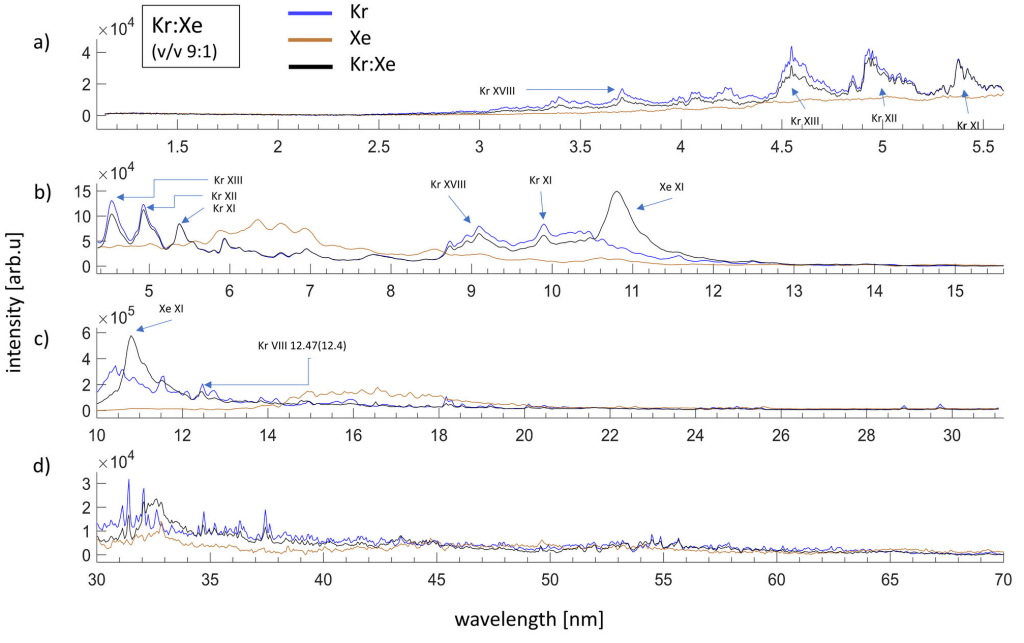

Fig. 10. Kr:Xe (v/v 9:1) spectra in the wavelength range of: a) 1–5 nm, b) 4–15 nm, c) 10–32 nm, and d) 30–70 nm. Individual Kr and Xe spectra are overlapped for comparison with the mixture emission.

Metrol. Meas. Syst., Vol. 27 (2020), No. 4, pp. 701–719
DOI: 10.24425/mms.2020.134848

target is due to strong reabsorption of the line by the cold Xe outside the interaction region. In the case of the Kr:Xe mixture the amount of reabsorbing Xe is much smaller due to the composition of the mixture, thus this effect is reduced and emission in this region can be detected. It can also be noticed from a comparison in the region 5.5 nm to 8.6 nm that the individual Xe emission slightly dominates over the emission from the Kr:Xe mixture. The most intense arrays of transitions were identified. In the EUV II range third diffraction order of the spectral band related to the 10 nm band is detected and identified in Fig. 10d.

A mixture of methane, carbon dioxide, and nitrogen, (C–Z = 6, *H*–Z = 1, O–Z = 8, and N–Z = 7) in equal proportions, was also investigated. The results of the investigation are shown with a comparison of emissions from CO_2 alone in Fig. 11a–d. Apart from the characteristic lines of oxygen and nitrogen in the SXR region, we also identified brighter carbon lines corresponding to C-V and C-VI. In the EUV I region we were able to detect emission from C-VI, O-VI and second diffraction order lines corresponding to N-VI and C-V ionization levels. In the EUV II region, spectral lines corresponding to N-V and O-V to O-VI ionization levels are detected.

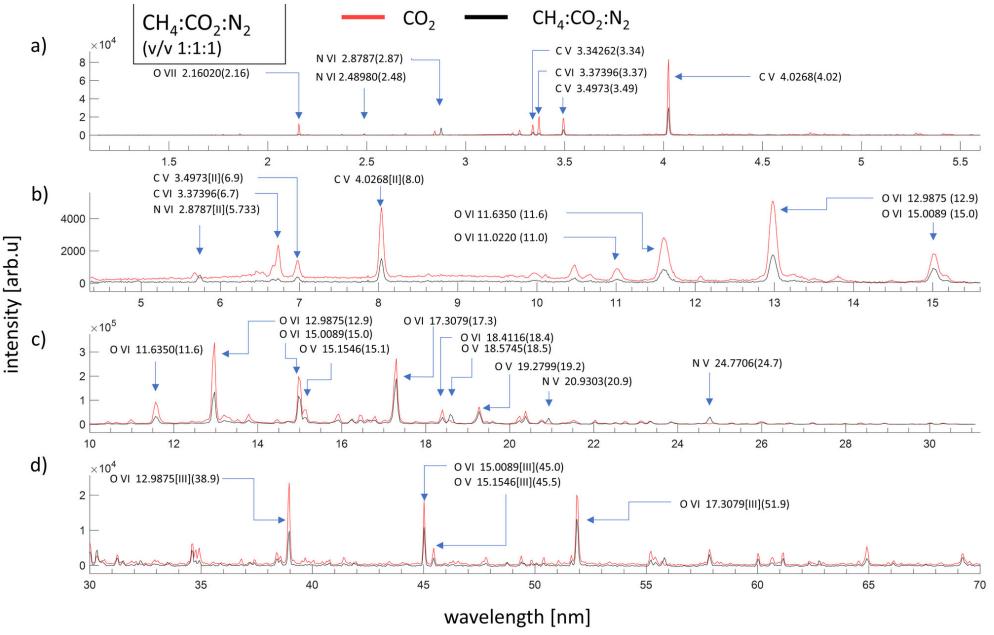

Fig. 11. CH_4: CO_2: N_2 (v/v 1:1:1) spectra in the wavelength range of: a) 1–5 nm, b) 4–15 nm, c) 10–32 nm, and d) 30–70 nm. CO_2 gas spectra are overlapped for comparison with the mixture emission.

Results for emission from a mixture of argon, nitrogen, and oxygen (Ar – Z = 18, O – Z = 8, and N–Z = 7) in equal volumetric proportions with a comparison of emission from individual gases are given in Fig. 12a–d. In the spectrum, almost all the lines which were previously attributed to the individual gases were identified. The SXR spectral lines are predominantly from Ar-IX and Ar-X ions in addition to characteristic lines from oxygen and nitrogen ions. In the EUV I region, Ar-IX, Ar-VII, and O-VI lines were identified. In the EUV II region, argon and oxygen emissions are equally dominant in terms of intensity of lines though nitrogen emission is comparatively weak. In this region, we identified lines corresponding to Ar-VII to Ar-IX, O-V, O-VI, and N-V ionization states. A comparison between emissions from the individual gas target and mixed gas targets in Fig. 12c provides insight into the peculiarities of their emissions. The O-VI line

emission at 12.9 nm from individual O_2 gas is higher compared to that from its mixture, while the O-VI line emissions from both mixed and individual O_2 gas targets at 17.3 nm have similar intensity levels.

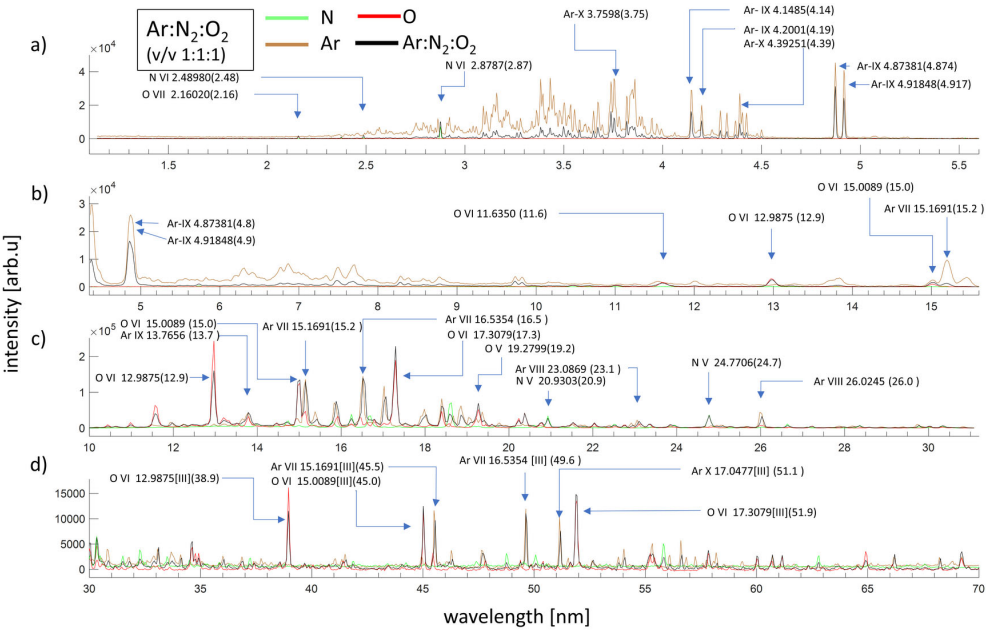

Fig. 12. Ar: N_2: O_2 (v/v 1:1:1) spectra in the wavelength range of: a) 1–5 nm, b) 4–15 nm, c) 10–32 nm, and d) 30–70 nm. Individual gas spectra of Ar, O_2, and N_2 are also overlapped for comparison with the mixture emission.

All the data presented in Figs. 2–12 are available in Excel format as a supplementary material.

4. Discussions and conclusions

The general nature of spectral plots in the 10–70 nm spectral range (EUV II spectrometer) shows that more intense lines are seen towards the left side of the spectra (energies around 10–20 nm) and are a consequence of the achievable power density (defined by the laser pulse energy, pulse duration, and focal spot area) in this particular experiment.

The use of a mixture of gases as a target has several advantages. Mixing of gases with characteristic spectral lines is one of the techniques for easier calibration of spectrometers in the broader spectral range. For the optical coherence tomography applications, in which a broad spectral emission band is required, emissions from component gases can be complimentary for producing a broad emission band in the EUV or SXR range, dedicated to the XCT acquisitions. We could see such bands in the mixture of Kr and Xe around the 8–12 nm wavelength range. Emission from specific wavelength regions can be enhanced by proper optimization for that region. Mixing of gases is also important to increase the fluence from spectral lines by taking advantage of Penning ionization [35], hence one of the possible tasks for the future is to simulate and optimize the ratio of the concentration of gases in mixtures to increase gas density while minimizing the reabsorption of specific lines. Specifically, for X-ray coherent tomography applications, optimization of individual gas concentrations in the mixture for a uniform broadband emission may provide better axial

resolution. Such studies can also contribute to finding optimized mixtures for suppression of particular wavelengths to produce quasi-monochromatic emissions which can be advantageous in SXR microscopy and EUV lithography applications where highly narrowband emissions are preferred.

DGPT-based laser plasma sources for the above-mentioned applications warrant very fine adjustments to optimize the emission output in accordance with the applications and wavelength range of significance. The results point to a need for a larger analysis of each ionization stage of every gas and its use in order to characterize the source and generated plasma conditions for each species. Optimization of laser energy to produce optimum plasma conditions for maximizing emission at specific wavelength ranges is also to be conducted according to requirements of specific applications. Generally, low-Z number gases have very fine spectra composed of isolated emission lines which are particularly suitable for experiments requiring quasi-monochromatic spectrum (EUV/SXR microscopy, metrology, radiography for density estimation of gases, holography), whereas higher atomic number gases which can emit broader spectra in these regions, can be used for applications requiring polychromatic emissions such as NEXAFS, EXAFS, X-ray coherence tomography or other applications for which the large number of photons is a priority, *e.g.* contact microscopy. While the presented results give a qualitative analysis of the emission spectra, they could also be used to simulate or optimize the emission for specific applications.

One of the most important applications of the results presented is characterization of plasma parameters for different gas targets in laser-produced plasma experiments in a broad spectral range. Since the plasma phenomenon occurs over a range of several nanoseconds, the acquired spectra are a time-integrated spectral response. Different stages of ionization occur which emit radiations from visible to SXR range during the laser pulse. To execute a structured and wider analysis in terms of plasma parameters for each gas and each wavelength range, one should engage at least in sub-ns time-resolved spectral studies and estimate the temperature and the density separately, tracing those parameters as the plasma evolves in time. Such measurements were already performed [36], but only for a single gas mixture and in the limited spectral range.

However, overall time-integrated estimations for plasma parameters can still be evaluated. By analyzing relative intensities using Boltzmann plots [37] for different ions such as N-VI, C-VI, C-V, in the SXR range and O-VI and N-V in the EUV range, we were able to approximately estimate electron temperature ranging from 90 eV to 110 eV in the SXR range and 37 eV to 52 eV in the EUV range. We found that the estimated values were in accordance with the simulations performed using the Z* code [38]. Using FLYCHK simulation software we also found relations between electron temperature and atomic level population and ionization distributions [39]. The electron density considered for the simulations is in the range 1×10^{17} to 1×10^{18} cm^3. Any visible radiation originating from the cooler portions of the plasma was not considered in the present study.

In conclusion, we have presented spectral measurements of a laser-plasma EUV/SXR source based on double gas puff targets. We have evaluated emission from eleven gases and gas mixtures which might be used as gas targets for laser-matter interaction forming a plasma, emitting radiation in a broad wavelength range from 1 nm up to 70 nm wavelength (photon energy from 18 eV to 1240 eV).

Funding

The research was funded by the National Science Centre (NCN) (2016/23/G/ST2/04319, UMO-2015/17/B/ST7/03718, and UMO-2015/19/B/ST3/00435); European Union's Horizon 2020 research and innovation program Laserlab-Europe V (871124).

References

[1] International Organization for Standardization. (2007). *Space environment (natural and artificial) – Process for determining solar irradiances* (ISO 21348:2007). https://www.iso.org/standard/39911.html.

[2] Hotta, E., Sakai, Y., Zhu, Q., Huang, B., Kumai, H., & Watanabe, M. (2011). EUV and SXR sources based on discharge produced plasma. *2011 Academic International Symposium on Optoelectronics and Microelectronics Technology*, 4–7. https://doi.org/10.1109/AISMOT.2011.6159301

[3] Malm, E. B., Monserud, N. C., Brown, C. G., Wachulak, P. W., Xu, H., Balkrishnan, G., Chao, W., Anderson, E., & Marconi, M. C. (2013). Tabletop single-shot extreme ultraviolet Fourier transform holography of an extended object. *Optics Express, 21*(8), 9959–9966. https://doi.org/10.1364/OE.21.009959

[4] Bravo, H., Szapiro, B. T., Wachulak, P. W., Marconi, M. C., Chao, W., Anderson, E. H., Menoni, C. S., & Rocca, J. J. (2011). Demonstration of nanomachining with focused extreme ultraviolet laser beams. *IEEE Journal of Selected Topics in Quantum Electronics, 18*(1), 443–448. https://doi.org/10.1109/JSTQE.2011.2158392

[5] Niemann, B., Rudolph, D., & Schmahl, G. (1976). X-ray microscopy with synchrotron radiation. *Applied Optics, 15*(8), 1883–1884. https://doi.org/10.1364/AO.15.001883

[6] Jacobsen, C., & Kirz, J. (1998). X-ray microscopy with synchrotron radiation. *Nature Structural Biology, 5*(8), 650–653. https://doi.org/10.1038/1341

[7] Rumsby, P. T. (1985). Laser produced plasmas as intense X-ray sources for microscopy at the Central Laser Facility. *Journal of Microscopy, 138*(3), 245–265. https://doi.org/10.1111/j.1365-2818.1985.tb02619.x

[8] Bartnik, A., Wachulak, P., Fok, T., Wegrzyński, L., Fiedorowicz, H., Pisarczyk, T., Chodukowski, T., Kalinowska, Z., Dudzak, R., Dostal, J., Krousky, E., Skala, J., Ullschmied, J., Hrebicek, J., & Medrik, T. (2015). Photoionized plasmas induced in neon with extreme ultraviolet and soft X-ray pulses produced using low and high energy laser systems. *Physics of Plasmas, 22*, 043302. https://doi.org/10.1063/1.4919024

[9] Trail, J. A., & Byer, R. L. (1989). Compact scanning soft-x-ray microscope using a laser-produced plasma source and normal-incidence multilayer mirrors. *Optics Letters, 14*(11), 539–541. https://doi.org/10.1364/OL.14.000539

[10] Su, M. G., Min, Q., Cao, S. Q., Sun, D. X., Hayden, P., O'sullivan, G., & Dong, C. Z. (2017). Evolution analysis of EUV radiation from laser-produced tin plasmas based on a radiation hydrodynamics model. *Scientific Reports, 7*, 45212. https://doi.org/10.1038/srep45212

[11] Fujimoto, J., Hori, T., Yanagida, T., Ohta, T., Kawasuji, Y., Shiraishi, Y., Abe, T., Kodama, T., Nakarai, H., Yamzaki, T., & Mizoguchi, H. (2012). Development of laser-produced plasma-based EUV light source technology for HVM EUV lithography. *Extreme Ultraviolet (EUV) Lithography III*, 8322. https://doi.org/10.1117/12.916093

[12] Malmqvist, L., Rymell, L., Berglund, M., & Hertz, H. M. (1996). Liquid-jet target for laser-plasma soft x-ray generation. *Review of Scientific Instruments, 67*(12), 4150–4153. https://doi.org/10.1063/1.1147561

[13] Fiedorowicz, H., & Bartnik, A. (2005). X-ray laser emission from a laser-irradiated gas puff target. *Bulletin of the Polish Academy of Sciences: Technical Sciences, 53*(2), 103–111. https://journals.pan.pl/Content/111758/PDF/%2853-2%29103.pdf.

[14] Chkhalo, N. I., Garakhin, S. A., Lopatin, A. Ya., Nechay, A. N., Pestov, A. E., Polkovnikov, V. N., Salashchenko, N. N., Tsybin, N. N., & Zeuv, S. Yu. (2018). Conversion efficiency of a laser-plasma source based on a Xe jet in the vicinity of a wavelength of 11 nm. *AIP Advances, 8*(10), 105003. https://doi.org/10.1063/1.5048288

Metrol. Meas. Syst., Vol. 27 (2020), No. 4, pp. 701–719
DOI: 10.24425/mms.2020.134848

[15] Banine, V., & Moors, R. (2004). Plasma sources for EUV lithography exposure tools. *J. Phys. D: Appl. Phys., 37*(23), 3207–3212. https://doi.org/10.1088/0022-3727/37/23/001

[16] Tallents, G. J. (2019). Opacity effects on laser-produced plasma radiation sources. *Journal of Applied Physics, 126*(8). https://doi.org/10.1063/1.5111720

[17] Fiedorowicz, H., Bartnik, A., Jarocki, R., Rakowski, R., & Szczurek, M. (2000). Enhanced X-ray emission in the 1-keV range from a laser-irradiated gas puff target produced using the double-nozzle setup. *Applied Physics B, 70*(2), 305–308. https://doi.org/10.1007/s003400050050

[18] Wachulak, P., Bartnik, A., & Fiedorowicz, H. (2010). Sub-70 nm resolution tabletop microscopy at 13.8 nm using a compact laser–plasma EUV source. *Optics Letters, 35*(14), 2337–2339. https://doi.org/10.1364/OL.35.002337

[19] Wachulak, P., Bartnik, A., Skorupka, M., Kostecki, J., Jarocki, R., Szczurek, M., Wegrzyński, L., Fok, T., & Fiedorowicz, H. (2013). Water-window microscopy using a compact, laser-plasma SXR source based on a double-stream gas-puff target. *Applied Physics B, 111*(2), 239–247. https://doi.org/10.1007/s00340-012-5324-y

[20] Wachulak, P., Duda, M., Fok, T., Bartnik, A., Wang, Z., Huenag, Q., Sarzyński, A., Jancarek, A., & Fiedorowicz, H., (2018). Single-shot near edge X-ray absorption fine structure (NEXAFS) spectroscopy using a laboratory laser-plasma light source. *Materials, 11*(8), 1303. https://doi.org/10.3390/ma11081303

[21] Wachulak, P., Bartnik, A., Jarocki, R., & Fiedorowicz, H. (2012). Characterization of multi-jet gas puff targets for high-order harmonic generation using EUV shadowgraphy. *Nuclear Instruments and Methods in Physics Research Section B: Beam Interactions with Materials and Atoms, 285*, 102–106. https://doi.org/10.1016/j.nimb.2012.05.006

[22] Bartnik, A., Fiedorowicz, H., Jarocki, R., Kostecki, J., Szczurek, M., & Wachulak, P. (2011). Laser-plasma EUV source dedicated for surface processing of polymers. *Nuclear Instruments and Methods in Physics Research Section A: Accelerators, Spectrometers, Detectors and Associated Equipment, 647*(1), 125–135. https://doi.org/10.1016/j.nima.2011.05.033

[23] Wachulak, P., Bartnik, A., & Fiedorowicz, H. (2018). Optical coherence tomography (OCT) with 2 nm axial resolution using a compact laser plasma soft X-ray source. *Scientific Reports, 8*(1). https://doi.org/10.1038/s41598-018-26909-0

[24] Sizyuk, V., Hassanein, A., Morozov, V., Tolkach, V., Sizyuk, T., Rice, B. (2006). Numerical Simulation of Laser-Produced Plasma Devices for EUV Lithography Using the Heights Integrated Model. *Numerical Heat Transfer, Part A: Applications, 49*(3), 215–236. https://doi.org/10.1080/10407780500324996

[25] O'Sullivan, G., Li, B., D'Arcy, R., Dunne, P., Hayden, P., Kilbane, D., McCormack, T., Ohashi, H., O'Reilly, F., Sheridan, P., Sokell, E., Suzuki, C., & Higashiguchi, T. (2015). Spectroscopy of highly charged ions and its relevance to EUV and soft x-ray source development. *Journal of Physics B: Atomic, Molecular and Optical Physics, 48*(14). https://doi.org/10.1088/0953-4075/48/14/144025

[26] Masnavi, M., & Parchamy, C. (2019). Calculation of extreme-ultraviolet radiation conversion efficiency from a laser-produced tin plasma source. *Physics Open, 1*, 100003. https://doi.org/10.1016/j.physo.2019.100003

[27] Berglund, M., Rymell, L., Peuker, M., Wilhein, T., & Hertz, H. M. (2000). Compact water-window transmission X-ray microscopy. *Journal of Microscopy, 197*(3), 268–273. https://doi.org/10.1046/j.1365-2818.2000.00675.x

[28] Ayele, M., Wachulak, P., Czwartos, J., Adjei, D., Bartnik, A., Wegrzyński, Ł., Szczurek, M., Pina, L., & Fiedorowicz, H. (2017). Development and characterization of a laser-plasma soft X-ray source for contact microscopy. *Nuclear Instruments and Methods in Physics Research Section B: Beam Interactions with Materials and Atoms, 411*, 35–43. https://doi.org/10.1016/j.nimb.2017.03.082

[29] Michette, A. G. (1989). Laser-generated plasmas: Source requirements for X-ray microscopy. *Proc. SPIE 1140, X-Ray Instrumentation in Medicine and Biology, Plasma Physics, Astrophysics, and Synchrotron Radiation*, France, 289–296. https://doi.org/10.1117/12.961838

[30] Fuchs, S., Rödel, C., Blinne, A., Zastrau, U., Wünsche, M., Hilbert, V., Glaser, L., Viefhaus, J., Frumker, E., Corkum, P., Förster, E., & Paulus, G. (2016). Nanometer resolution optical coherence tomography using broad bandwidth XUV and soft x-ray radiation. *Scientific Reports, 6*, 20658. https://doi.org/10.1038/srep20658

[31] Gray, W. J., Keiter, P. A., Lefevre, H., Patterson, C. R., Davis, J. S., Powell, K. G., Kuranz, C. C., & Drake. R. P. (2019). Atomic modelling of photoionization fronts in nitrogen gas. *Physics of Plasmas, 26*(5), 052901. https://doi.org/10.1063/1.5090803

[32] Wachulak, P., Duda, M., Bartnik, A., Sarzyński, A., Wegrzyński, Ł., Nowak, M., Jancarek, A., & Fiedorowicz, H. (2018). Compact system for near edge X-ray absorption fine structure (NEXAFS) spectroscopy using a laser-plasma light source. *Optics Express, 26*(7), 8260–8274. https://doi.org/10.1364/OE.26.008260

[33] Kramida, A., Ralchenko, Yu., Reader, J. & NIST ASD Team (2020). NIST Atomic Spectra Database (version 5.8). https://doi.org/10.18434/T4W30F

[34] Kelly, R. L. (1973). Atomic and ionic emission lines below 2000 Angstroms, hydrogen through krypton. NRL Report 7599, *Naval Research Laboratory*, Washington. https://doi.org/10.2172/6644558

[35] Morgner, H., & Niehaus, A. (1979). Experimental and theoretical study of the Penning ionisation of H atoms by He metastables. *Journal of Physics B: Atomic and Molecular Physics, 12*(11), 1805. https://doi.org/10.1088/0022-3700/12/11/008

[36] Saber, I., Bartnik, A., Wachulak, P., Skrzecznowski, W., Jarocki, R., & Fiedorowicz, H. (2017). Temporal variations of electron density and temperature in Kr/Ne/H2 photoionized plasma induced by nanosecond pulses from extreme ultraviolet source. *Physics of Plasmas, 24*, 063501. https://doi.org/10.1063/1.4984254

[37] Aguilera, J. A., & Aragon, C. (2007). Multi-element Saha-Boltzmann and Boltzmann plots in laser-induced plasmas. *Spectrochimica Acta Part B: Atomic Spectroscopy, 62*(4), 378–385. https://doi.org/10.1016/j.sab.2007.03.024

[38] Zakharov, S. V., Novikov, V. G., & Choi, P. (2006). Z*-code for DPP and LPP source modeling. In Bakshi, V. (Eds.), *EUV Sources for Lithography*. Spie Press. https://doi.org/10.1117/3.613774.Ch8

[39] Lung, H. K., Chen, M. H., Morgan, W. L., Ralchenko, Y., & Lee, R. W. (2005). FLYCHK: Generalized population kinetics and spectral model for rapid spectroscopic analysis for all elements. *High Energy Density Physics*, 1(1), 3–12. https://doi.org/10.1016/j.hedp.2005.07.001

Antony Jose Arikkatt received his M.Sc degree in optical engineering from Warsaw University of Technology (WUT), Poland in 2018. He is currently pursuing his Ph.D degree in X-ray coherence tomography in Military University of Technology (WAT), Warsaw, Poland. His main interests are in X-ray optics, laser plasma, plasma physics and holography.

Przemyslaw W. Wachulak obtained his M.Sc. degree in Electrical and Computer Engineering, major: laser technology, from the Military University of Technology (MUT), Warsaw, Poland in 2004 and his Ph.D. degree in Electrical and Computer Engineering, major: extreme ultraviolet technology, from the Colorado State University (CSU), Fort Collins, Colorado, USA in 2008, habilitation degree in physics in 2013 from the University of Warsaw, and Full Professorship in 2018. Currently he holds position of the rector-commandant of the Military University of Technology. His work focuses on the development of new laser-plasma sources for the generation of extreme ultraviolet and soft X-ray radiation for applications in nanoimaging, holography, absorption spectroscopy, optical coherence tomography, or radiobiology.

Metrol. Meas. Syst., Vol. 27 (2020), No. 4, pp. 701–719
DOI: 10.24425/mms.2020.134848

Joanna Czwartos obtained the PhD degree in physics at Department of Physics of Adam Mickiewicz University, Poznań, Poland in 2009. She is currently Assistant Professor at Institute of Optoelectronics of Military University of Technology, Warsaw, Poland. Her research activity focuses on examination of effect of extreme ultraviolet (EUV) and photoionizing plasma radiation on physicochemical properties and cytocompatiblity of various organic polymers.

Andrzej Bartnik received his Ph.D. degree from Military University of Technology, Warsaw, Poland, in 1996, in material engineering and D.Sc. degree from Military University of Technology, in 2016 in electronics. Currently holds position of an associate professor at the Institute of Optoelectronics, MUT, Warsaw, Poland. His main interests are: development of laser-produced plasma soft X-ray and extreme ultraviolet sources, research concerning interaction of high intensity ionizing radiation with matter, micromachining and surface modification of solids, creation and investigation of photoionized plasmas.